PHYSICAL REVIEW B **110**, 104414 (2024)

Classical spin models and basic magnetic interactions on 1/1-approximant crystals

Daniel Qvarngård[1,*] and P. Henelius[1,2]
[1]*Department of Physics, Royal Institute of Technology, SE-106 91 Stockholm, Sweden*
[2]*Faculty of Science and Engineering, Åbo Akademi University, 20500 Åbo, Finland*

(Received 15 November 2023; accepted 21 June 2024; published 9 September 2024)

We study classical spin models on the 1/1 Tsai-type approximant lattice using Monte Carlo and mean-field methods. Our aim is to understand whether the phase diagram differences between Gd- and Tb-based approximants can be attributed to anisotropy induced by the crystal-electric field. To address this question, we treat Gd ions as Heisenberg spins and Tb ions as Ising spins. Additionally, we consider the presence of the Ruderman-Kittel-Kasuya-Yosida (RKKY) interaction to replicate the experimentally observed correlation between magnetic properties and electron concentration. Surprisingly, our findings show that the transition between ferromagnetic and antiferromagnetic order remains unaltered by the anisotropy, even when accounting for the dipole interaction. We conclude that a more comprehensive model, extending beyond the free-electron gas RKKY interaction, is likely required to fully understand the distinctions between Gd- and Tb-based approximants. Our work represents a systematic exploration of the impact of anisotropy on the ground-state properties of classical spin models in quasicrystal approximants.

DOI: 10.1103/PhysRevB.110.104414

I. INTRODUCTION

Quasicrystals provide a unique setting to theorists and experimentalists alike; as well as having crystallographically forbidden rotational symmetries, quasicrystals possess macroscopic structural order that never repeats [1–3]. As most of solid-state physics relies on periodicity, there is considerable difficulty in adapting existing methods to treat quasiperiodic systems. However, a possible stepping stone towards studying quasicrystals presents itself in the form of approximants, which are sequences of periodic materials with increasing unit cell sizes. Locally, their structure is the same as that of the limiting quasicrystal; if the correlation length of the observables of interest is shorter than the size of the unit cell, then one would therefore expect the physical properties to be similar. Furthermore, a thorough understanding of the properties of the approximants is necessary to identify what makes the quasiperiodic phase unique. In this paper, we present a theoretical study of classical spin models on a Tsai-type approximant as a baseline for further work on their magnetic properties.

Tsai-type materials [4] are a class of complex intermetallics which can occur both in quasicrystalline form and as periodic approximants. The materials contain at least two different elements [5] and are built from clusters of several concentric polyhedral shells. Of particular interest is the icosahedral shell, which can host the magnetic rare-earth elements. Since the discovery of Tsai-type clusters containing rare-earth elements there has been extensive research into their magnetic properties, with the main focus on finding a quasiperiodic system with long-range magnetic order [6]. A quasicrystalline ferromagnet was found by Tamura *et al.* [7] in a Tsai-type Au-Si-Tb system in 2021, but antiferromagnetic order is yet to be observed in quasicrystals despite antiferromagnetic phases being allowed by symmetry arguments [8].

As Tsai-type quasicrystals are difficult to investigate from both theoretical and experimental viewpoints, a recurring theme has been to study the periodic approximants to determine which parameter ranges to prioritize in the pursuit of quasiperiodic magnetic order [9,10]. The approximants are labeled by a rational number approximating the golden ratio, $\tau = (1 + \sqrt{5})/2$. Simplest among the approximants are the 1/1 approximants, which resemble body-centered cubic lattices decorated with Tsai-type clusters; see Fig. 1 for the magnetic lattice. For the rest of this paper, the word approximant is strictly referring to a 1/1 Tsai-type approximant.

Suzuki *et al.* noted that the Curie-Weiss temperature, which is proportional to the mean magnetic coupling, varies with the conduction electron density for a set of ternary approximant materials [11]. We reproduce their result in Fig. 2, where we have modified the abscissa to represent the Fermi wave vector as estimated by Eq. (6). There is a critical value for k_F below which Tb-based approximant samples transition from ferromagnetic (FM) to antiferromagnetic (AFM) [12]. However, Gd-based approximants favor FM order, and their transition point is at a much lower electron concentration than their Tb counterparts in spite of the similarities in Curie-Weiss temperatures. The leading hypothesis is that this is due to the difference in on-site anisotropies experienced by Gd and Tb ions [13].

The simplest way to model the conduction electrons is to treat them as a Fermi gas with a spherical Fermi surface which

---

[*] Contact author: danielqv@kth.se

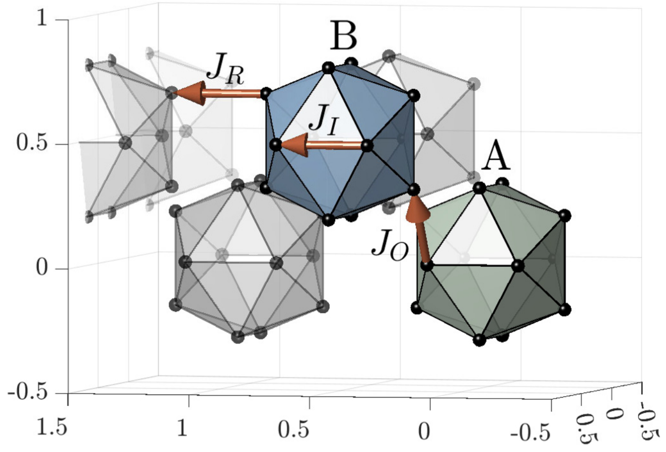

FIG. 1. Geometry of the cubic unit cell, in units of the lattice parameter. Rare-earth sites occur on the vertices of the icosahedra, which in turn are centered at $(0, 0, 0)$ (labeled "A") and $(1/2, 1/2, 1/2)$ (labeled "B"), respectively. Clusters from outside the unit cell are grayed out. J_O, J_I, and J_R denote the three nonequivalent nearest-neighbor distances we consider for the direct exchange terms; see Sec. II C.

is coupled to the rare-earth magnetic moments through an antiferromagnetic exchange term. This gives rise to an effective coupling between the rare-earth moments: the Ruderman-Kittel-Kasuya-Yosida (RKKY) interaction [14–16]. Sugimoto *et al.* [17] presented a phenomenological model of approximants based on the RKKY interaction and easy-plane anisotropy, which reproduces magnetic states observed in neutron diffraction experiments on Tb-Au-Si approximants. Miyazaki *et al.* [18] investigated classical Heisenberg spins interacting through RKKY; the resulting ground-state phase diagram as a function of electron concentration correlates with that found in experiments.

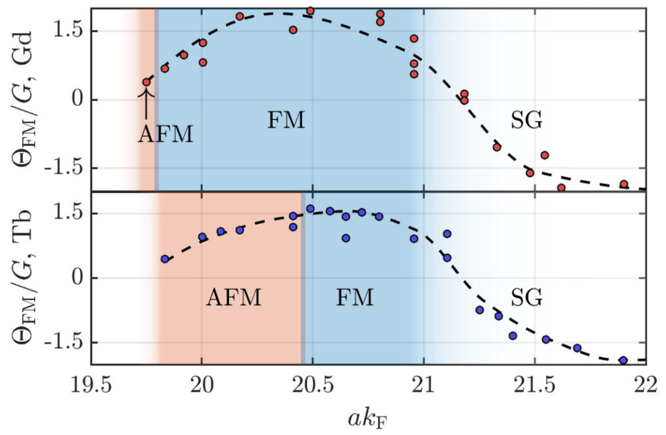

FIG. 2. Experimentally measured reduced Curie-Weiss temperatures in Kelvin for Gd-based (top, red dots) and Tb-based (bottom, blue dots) 1/1-approximants versus ak_F, lattice constant a times the Fermi wave vector k_F. Background colors illustrate an approximate magnetic phase diagram. The ordinate values have been divided by the de Gennes factor; see Eq. (5) and the following discussion. Dashed lines are guides to the eye. Adapted from Suzuki *et al.* [11].

In this work, we study classical spin models on the Tsai-type 1/1 approximant lattice using a Monte Carlo approach. We investigate the magnetic properties under the RKKY interaction, but we also consider direct exchange and dipole-dipole interactions in a systematic fashion. In order to connect the simulations to neutron diffraction results, focus lies on the ground-state properties of each class of interaction as well as on investigating how the phase diagram under the RKKY interaction is affected by including the direct exchange and dipole interactions. Furthermore, we introduce an Ising ansatz to model the crystal field effect on Tb to determine if strong anisotropy has an effect on the magnetic properties. This model has easy-axis anisotropy, and we contrast it against the case of the isotropic Heisenberg spin symmetry as a model for Gd. Understanding the difference between Tb- and Gd-based approximants could be important for synthesizing magnetic quasicrystals, as approximants have a greater parameter range where they are thermodynamically stable compared to their quasicrystalline counterpart. Therefore, understanding how different rare-earth ions behave in Tsai-type clusters could be important for engineering the quasicrystal magnetic properties [6].

The paper is organized as follows: In Sec. II, we introduce our model, starting with the lattice geometry, followed by a discussion of the easy-axis model we employ for the crystal electric field, before ending on a presentation of the Hamiltonians under study. In Sec. III, we describe our Monte Carlo approach. The results are presented and discussed in Sec. IV, where we begin by determining the magnetic properties of the direct exchange, RKKY and dipole terms separately. Finally, we consider how dipole and direct exchange terms influence the RKKY ground states as the Fermi wave vector is changed.

II. MODEL

A. Lattice

If rare-earth ions are present in the Tsai-type 1/1 approximant, then they are located at the positions shown as vertices in Fig. 1. The magnetic lattice is a body-centered cubic (BCC) arrangement of clusters of rare-earth ions, which are in turn located on the vertices of icosahedra. The vertices of an icosahedron can be represented by the cyclic permutations of the position vector $\mathbf{r}_i \propto (\pm 1 \pm \tau\ 0)$, where $\tau = (1 + \sqrt{5})/2$ is the golden ratio. The cubic unit cell parameter, a, is approximately 15 Å. In this work we take the radius of the icosahedral clusters to be $r_{\mathrm{Ico}} \approx 0.365a$.

The full decoration of the BCC unit cell is made up of a series of concentric shells; an illustration is provided by Suzuki *et al.* [11]. The icosahedra containing rare-earth ions are surrounded by shells containing Au and Si. For our purpose, the key property is this: Certain lattice sites are partially occupied by either Au or Si, and this occupancy can be tuned by sample composition. As Au and Si have different valency, one can synthesize materials with different conduction electron density, which we model with a corresponding Fermi wave vector. In spite of the disordered nature of the materials we aim to study, we take the icosahedra to be perfectly symmetric and of the same radius throughout the lattice.

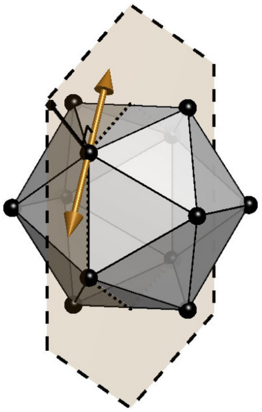

FIG. 3. Spin symmetry of the Ising kind. Transparent hexagon denotes a mirror plane of the lattice, thick black line the normal vector of the icosahedral cluster, and orange vectors show the two possible choices of directions for the Ising spin $\mathbf{S}_i$.

B. Spin symmetry

The crystal electric field in real materials typically induces a magnetic anisotropy depending on the orbital states of the electrons in the unfilled ionic shells. Thus, the local magnetic moments have a set of preferred directions. In this study, our starting point is to neglect the anisotropy and model the ionic magnetic moments as classical Heisenberg spins. This model should approximate the behavior of Gd-based compounds: By Hund's rules, the electronic ground state of a free Gd ion has zero orbital angular momentum and its $4f$-electron density is spherically symmetric; therefore the crystal electric field will have little effect on its magnetic properties [19].

To study the hypothesis that the main difference between the Tb and Gd approximant phase diagrams is due to on-site anisotropy, we model the Tb moments as Ising spins pointing along the icosahedral cluster normal and inside a mirror plane of the lattice. For example, we assume the site at $\mathbf{r} \propto (\tau 1 0)$ has two possible choices for the Ising spin $\mathbf{S}_i \propto \pm(-1 \tau 0)$: see Fig. 3. We neglect any angular deviation from the idealized case discussed above as the point is not to match the actual anisotropy present in the material but to put our model in as stark a contrast to the Heisenberg symmetry as possible to maximize the difference in the observed phase diagram. We note, however, that magnetic structures close to those that are acquired from our ansatz have been derived as possible solutions in point charge model calculations as well as found through neutron scattering experiments on Tb-based approximants [20,21].

C. The Hamiltonian

We study the thermodynamic properties of classical Heisenberg and Ising model spins interacting via the Hamiltonian

$$\mathcal{H} = \mathcal{H}_{\mathrm{DE}} + \mathcal{H}_{\mathrm{RKKY}} + \mathcal{H}_{\mathrm{Dipole}}. \tag{1}$$

The class of terms contained in $\mathcal{H}_{\mathrm{DE}}$ are short-range direct exchange (DE) interactions of the exchange form,

$$\mathcal{H}_{\mathrm{DE}} = -\sum_{i,j} J_{ij}\mathbf{S}_i \cdot \mathbf{S}_j; \tag{2}$$

where $J_{ij} = 0$ if $|\mathbf{r}_{i,j}| \geqslant 0.39a$, and otherwise takes the values J_O for $|\mathbf{r}_{i,j}| \approx 0.360a$, J_I for $|\mathbf{r}_{i,j}| \approx 0.378a$, or J_R for $|\mathbf{r}_{i,j}| \approx 0.392a$ according to the relative placement of sites i and j according to Fig. 1. These three shortest distances are within ∼10% of one another, whereas the next shortest distance is approximately $0.532a$, and we neglect the corresponding direct exchange term. Given the bipartite nature of the lattice, the key geometrical observation is the following: Only J_O acts between sublattices A and B, whereas both J_I and J_R act within the same sublattice.

The RKKY interaction originates from the indirect exchange mediated by the conduction electrons, and is of the form [14–16]

$$\mathcal{H}_{\mathrm{RKKY}} = -J_{\mathrm{RKKY}} \sum_{|\mathbf{r}_{i,j}|<r_c} (2k_F r_{\mathrm{Ico}})^3 f(2k_F|\mathbf{r}_{i,j}|)\mathbf{S}_i \cdot \mathbf{S}_j, \tag{3}$$

where $r_c = 5a$ is a cutoff radius, k_F is the Fermi wave vector, and $f(r)$ is given by

$$f(r) = \frac{\sin(r) - r\cos(r)}{r^4}. \tag{4}$$

The presence of the cutoff of the RKKY interaction is motivated by disorder in the lattice: The effective range of the interaction is limited by the conduction electron mean-free path. As the Fermi wave vector is changed through doping, r_c should in principle correlate with k_F. However, we neglect this relation and instead choose a cutoff radius $r_c = 5a$, as we find convergence of our coupling constants at this point.

The relative strength of the RKKY interaction depends on the distance between the spins, the electron density, and the rare-earth element:

$$J_{\mathrm{RKKY}} = \frac{9\pi m_e J_{\mathrm{sf}}^2 \nu^2}{32\hbar^2 k_F^2} \frac{1}{(2k_F r_{\mathrm{Ico}})^3} G, \tag{5}$$

where ν is the number of valence electrons per atom, m_e is the electron mass, J_{sf} is a coupling constant between the conduction and f-shell electrons, and $G = (g-1)^2 J(J+1)$ is the de Gennes factor for total angular momentum modulus J (in units of $\hbar$). Neglecting partial occupancies, the total number of atoms per cubic unit cell is $N_a \approx 176$ [21], and the Fermi wave vector can be related to the electron-per-atom ratio ν as [22]

$$k_F = (3\pi^2 N_a \nu)^{1/3}/a. \tag{6}$$

In order to investigate the experimentally relevant interval $\nu \in [1, 2.2]$, we study the corresponding interval for the dimensionless parameter $ak_F \in [17, 22.5]$.

The dipolar interaction is defined by

$$\mathcal{H}_{\mathrm{Dipole}} = -J_D \sum_{i,j} r_{\mathrm{Ico}}^3 \frac{3(\mathbf{S}_i \cdot \hat{r}_{i,j})(\mathbf{S}_j \cdot \hat{r}_{i,j}) - \mathbf{S}_i \cdot \mathbf{S}_j}{|\mathbf{r}_{i,j}|^3}, \tag{7}$$

where $\hat{r}_{i,j}$ is the relative unit vector between sites i and j. Assuming free rare-earth ions, J_D is given by [19]

$$J_D = \frac{\mu_0}{4\pi} \frac{\mu_B^2}{r_{\mathrm{Ico}}^3} (gJ)^2. \tag{8}$$

Inserting values for Gd, we find $J_D \approx 0.2$ K, and for Tb, $J_D \approx 0.3$ K. Taking the typical value for the exchange parameter $J_{\mathrm{sf}} \sim 0.2$ eV in Eq. (5) [19], and m_e taken to be the free electron mass, the estimated magnitude for J_{RKKY} in Gd-based approximants is found to be ∼0.3 K—of comparable magnitude to J_D. Thus, we stress that we cannot neglect the dipole interaction *a priori*, as is usually done for, e.g., room-temperature ferromagnets [23].

III. METHODS

In this section we introduce the methods we use to analyze the properties of the terms in Eq. (1). To begin with, we reproduce the mean-field theory description of a bipartite Heisenberg model in Sec. III A. The purpose of this is twofold: First, it connects to the recent experimental focus on determining the Curie-Weiss temperature and, second, it provides an intuitively clear framework for explaining the transition between ferro- and antiferromagnetic order we observe in the Monte Carlo simulations, and in particular the role of the effective intersublattice coupling u_{AB}.

A. Mean-field theory

Consider a general Hamiltonian with scalar couplings,

$$\mathcal{H} = -\sum_{ij} J_{ij}\mathbf{S}_i \cdot \mathbf{S}_j. \tag{9}$$

In the framework of mean-field theory one neglects the correlations between spins, and each site interacts magnetically with the average field generated by the others. For Heisenberg spins, each site in Fig. 1 is equivalent by symmetry. Thus, one can make the ansatz that the z components of spins on the respective sublattices all have the same mean value: $\langle \mathbf{S}^z_{i\in A}\rangle = s_A$ and $\langle \mathbf{S}^z_{i\in B}\rangle = s_B$. The self-consistency condition for a spin at site i in the A sublattice becomes

$$s_A = \frac{\mathrm{Tr}_i[s_i e^{\beta(u_{\mathrm{AA}}s_A + u_{\mathrm{AB}}s_B + h_{\mathrm{ext}})s_i}]}{\mathrm{Tr}_i[e^{\beta(u_{\mathrm{AA}}s_A + u_{\mathrm{AB}}s_B + h_{\mathrm{ext}})s_i}]}, \tag{10}$$

where $\mathrm{Tr}_i(\cdot) = \int_{-1}^{+1} 2\pi\, ds_i(\cdot)$ is an integral over the possible orientations of $\mathbf{S}_i$ in a coordinate system where the local field is along the z axis, and the mean-field couplings are given by

$$u_{\mathrm{AA}} = \sum_{j\in A} J_{ij}, \quad i \in A, \tag{11}$$

describing the effective coupling within sublattices, and

$$u_{\mathrm{AB}} = \sum_{j\in B} J_{ij}, \quad i \in A, \tag{12}$$

describing the effective coupling between sublattices. There are analogous expressions for $i \in B$. By symmetry, $u_{\mathrm{BB}} = u_{\mathrm{AA}}$ and $u_{\mathrm{BA}} = u_{\mathrm{AB}}$. We use the letter u here as opposed to the customary J to distinguish the mean-field effective couplings from the model parameters in the Hamiltonian.

Computing the traces in Eq. (10) and expanding to linear order in β, one arrives at a matrix system for the average configurations,

$$\begin{bmatrix} u_{\mathrm{AA}} - 3/\beta & u_{\mathrm{AB}} \\ u_{\mathrm{BA}} & u_{\mathrm{BB}} - 3/\beta \end{bmatrix}\begin{bmatrix} s_A \\ s_B \end{bmatrix} = -h_{\mathrm{ext}}\begin{bmatrix} 1 \\ \sigma \end{bmatrix}, \tag{13}$$

where $\sigma = +1$ ($\sigma = -1$) probes for FM (AFM) order; see Eq. (22). Inverting the matrix and differentiating the resulting magnetization with respect to h_{ext}, one arrives at

$$\chi_{zz} \sim \frac{1}{1 - \beta(u_{\mathrm{AA}} + u_{\mathrm{AB}})/3}, \tag{14}$$

corresponding to $\sigma = +1$ in Eq. (13), and a staggered susceptibility

$$\chi_s \sim \frac{1}{1 - \beta(u_{\mathrm{AA}} - u_{\mathrm{AB}})/3}, \tag{15}$$

corresponding to $\sigma = -1$. In both cases, the critical temperature is given by

$$T_c \sim \frac{u_{\mathrm{AA}} + |u_{\mathrm{AB}}|}{3}. \tag{16}$$

A property of this mean-field solution that turns out to be important is the following: The sign of u_{AB} indicates whether one can expect a ferromagnet or an antiferromagnet, which we use to discuss the magnetic phase diagrams in Sec. IV [19].

B. Numerical methods

We use two different Monte Carlo approaches: the Metropolis algorithm [24] for Ising spins and the heat-bath [25] algorithm for Heisenberg spins. Unless otherwise noted, we simulate a system size of $24 \cdot 4^3 = 1536$ sites, i.e., a linear system size of $L = 4$ cubic unit cells. Furthermore, we employ periodic boundary conditions. In order to determine the ground state, we employ the simulated annealing approach using 10^6 updates per site and temperature and use a uniformly spaced distribution of 10 temperatures.

When simulating dipolar systems using periodic boundary conditions, care has to be taken as the series in Eq. (7) is in that case conditionally convergent. Any physical sample, however, has a boundary whose shape will influence the magnetostatic energy. The usual way to implement the boundary is through a shape-dependent Ewald sum, which for a spherically shaped sample yields the effective dipole Hamiltonian [26]

$$\mathcal{H}_D = -\frac{1}{2}J_D \sum_{i\neq j}(\mathbf{S}_i\cdot\nabla)(\mathbf{S}_j\cdot\nabla)\psi(\mathbf{r}_{ij}) + \mathcal{H}_{\mathrm{Boundary}}, \tag{17}$$

where the scalar potential is

$$\psi(\mathbf{r}) = \sum_{\mathbf{n}\in\mathbb{Z}^3} \frac{\mathrm{erfc}(\alpha|\mathbf{r}+\mathbf{n}|)}{|\mathbf{r}+\mathbf{n}|} + \sum_{|\mathbf{n}|\neq 0} \frac{1}{\pi|\mathbf{n}|^2} e^{2\pi i\mathbf{n}\cdot\mathbf{r}} e^{-\pi^2|\mathbf{n}|^2/\alpha^2}, \tag{18}$$

and $\mathcal{H}_{\mathrm{Boundary}}$ is given by

$$H_{\mathrm{Boundary}} = \frac{2\pi}{3}\frac{J_D}{L^3}\sum_{ij}\mathbf{S}_i\cdot\mathbf{S}_j. \tag{19}$$

The parameter α sets the convergence rate of the two different series in Eq. (18): A large α means that the first series requires fewer terms to converge and the second series requires more terms and vice versa. For our simulations, we used $\alpha = 1/L$ as an approximation to the optimal value for efficient calculation of ψ [27].

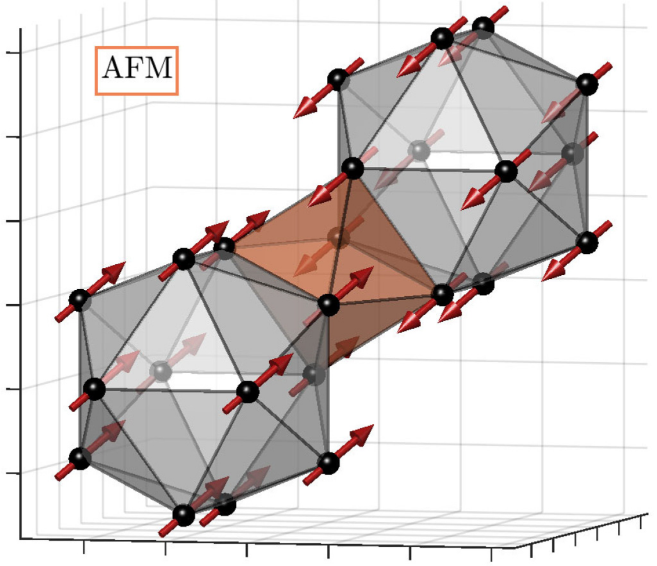

FIG. 4. An example AFM state which maximizes the staggered cluster magnetization $|\mathbf{M}_\mathbf{s}|$, and therefore also sublattice magnetization. Interstitial octahedron highlighted in orange to illustrate the depth, as the spins are staggered along the 111 direction.

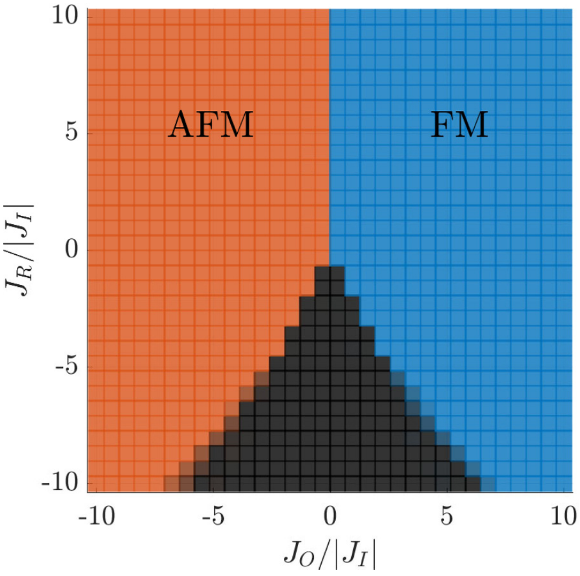

FIG. 5. Ground-state phase diagram for Heisenberg spin symmetry under $\mathcal{H}_{\mathrm{DE}}$ acquired via MC simulation. We have set $J_I = +1$, and modify the values of J_O and J_R along the x and y axis, respectively. Orange denotes antiferromagnetic order, and blue ferromagnetic order, as defined by Eqs. (20) and (22). Gray denotes states without a sublattice magnetization.

C. Observables under study

Using the methods described in Sec. III B, we calculate the thermal expectation values of a set of observables. To probe for FM order, we define the magnetization $\mathbf{M}$ as

$$\mathbf{M} = \sum_i \mathbf{S}_i, \tag{20}$$

and from the variance of the z component of the magnetization we define the differential susceptibility,

$$\chi_{zz} = \frac{\langle M_z M_z\rangle - \langle M_z\rangle \langle M_z\rangle}{N k_B T}. \tag{21}$$

As the lattice is of the BCC class with icosahedral clusters at the BCC sites, one can define a staggered cluster magnetization in analogy with undecorated BCC lattices,

$$\mathbf{M}_s = \sum_{i\in A} \mathbf{S}_i - \sum_{i\in B} \mathbf{S}_i, \tag{22}$$

where A and B are sublattices denoted by the corresponding letter in Fig. 1. An example of a state maximizing $|\mathbf{M}_s|$ is found in Fig. 4. Note that a state for which $\langle|\mathbf{M}_s|\rangle = 0$ could still have antiferromagnetic correlations between neighboring icosahedral clusters. For the purposes of this paper, however, antiferromagnetic order is defined as staggered magnetic order of the form given in Fig. 4.

IV. RESULTS AND DISCUSSION

In this section, we investigate the differences between the Heisenberg and Ising spin symmetries in the lattice in Fig. 1. With the numerical method outlined in Sec. III, we consider nearest neighbor, RKKY, and dipole interactions separately in Secs. IV A–IV C. Next, we consider the interplay between the RKKY and dipole terms in Sec. IV D, as the directional dependence in the dipole interaction might affect the symmetry properties of the ground states. Finally, we modify the intersublattice coupling u_{AB} by considering J_O and J_{RKKY} and study their mutual effect on the AFM/FM transition.

A. Direct-exchange interactions

We begin the presentation of our results by studying the short-range interactions in $\mathcal{H}_{\mathrm{DE}}$, Eq. (2). Although $\mathcal{H}_{\mathrm{DE}}$ does not capture the dependence of the magnetic properties on the electron concentration, its conceptual simplicity allows for direct comparison with mean-field theory. Furthermore, as chemical disorder provides an effective cutoff on the RKKY interaction, with a suitable choice of parameters $\mathcal{H}_{\mathrm{DE}}$ can be seen as a strong disorder limit of $\mathcal{H}_{\mathrm{RKKY}}$.

At zero temperature, only the relative magnitudes of couplings matter for the determination of the magnetic state. Thus, the only parameters determining the ground states of $\mathcal{H}_{\mathrm{DE}}$ are J_O/J_I, J_R/J_I, and the sign of J_I. Therefore, we consider the two cases $J_I = +1$ and $J_I = -1$ separately and study the ground state as a function of J_O and J_R using Monte Carlo simulation. As seen in Fig. 1, J_O sets the strength of the intersublattice coupling, i.e., $u_{\mathrm{AB}} \sim J_O$, whereas J_I and J_R contribute to the intrasublattice coupling u_{AA}. By requiring that $T_c > 0$ in Eq. (16), one can achieve a qualitative description of the phase boundaries of the nearest-neighbor Hamiltonian under Heisenberg symmetry: In the case of $J_I = +1$ and $J_R > 0$, Fig. 5, the magnetic ordering is determined by the sign of J_O, whereas when $J_R \lesssim -1$, larger magnitudes of J_O are needed to observe the AFM/FM ground states in order to overcome the negative u_{AA}. Similarly, when $J_I = -1$, the transitions occur at larger $|J_O|$; see Fig. 6. The actual parameter magnitudes at the phase boundaries do not

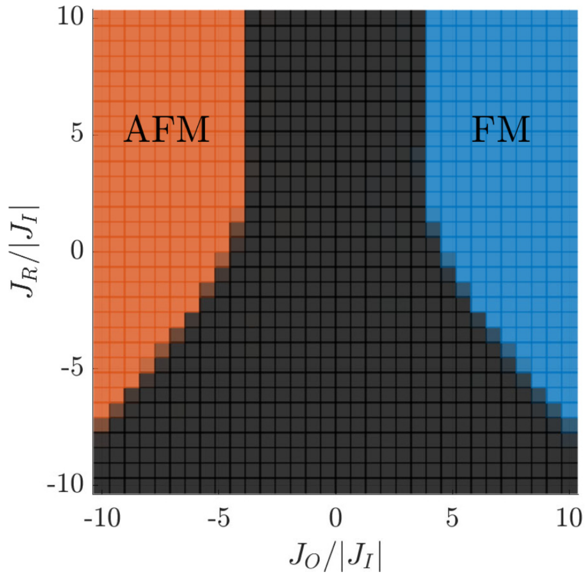

FIG. 6. Ground-state phase diagram for Heisenberg spin symmetry under $\mathcal{H}_{\rm DE}$ acquired via MC simulation. We have set $J_I = -1$, and modify the values of J_O and J_R along the x and y axis, respectively. Orange denotes antiferromagnetic order, and blue ferromagnetic order, as defined by Eqs. (20) and (22). Gray denotes states without a sublattice magnetization.

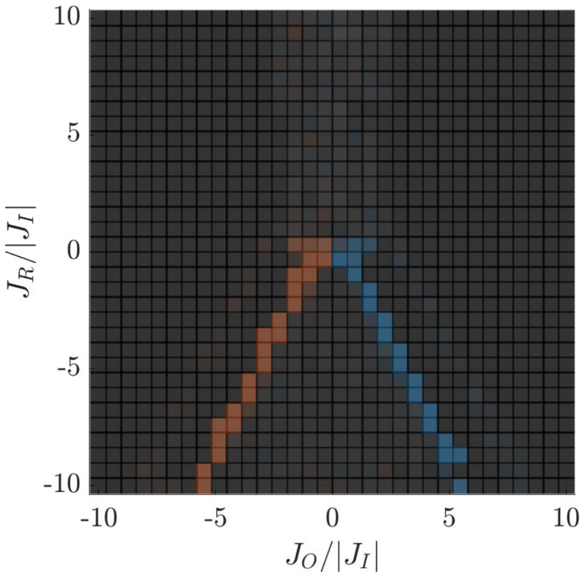

FIG. 7. Ground-state phase diagram for Ising spin symmetry under $\mathcal{H}_{\rm DE}$ acquired via MC simulation. We have set $J_I = +1$, and modify the values of J_O and J_R along the x and y axis, respectively. Orange denotes antiferromagnetic order, and blue ferromagnetic order, as defined by Eqs. (20) and (22). Gray denotes states without a sublattice magnetization. The axis of symmetry given by $J_O = 0$ persists as in Fig. 5, but magnetized states are only found in a Λ-shaped region.

agree with the estimates acquired from Eq. (16), which is likely due to the fact that the result for T_c is obtained via a high-temperature expansion and the exclusion of states with zero sublattice magnetization from our analysis.

The Ising-spin symmetry appears not to have finite values for the magnetization/staggered magnetization except when fine tuning the couplings; see Fig. 7, where we fix $J_I = +1$. We find magnetic order defined by Eqs. (20) and (22) only within thin lines in the regime where $J_R \leqslant 0$. It appears that the short-range interactions favor ground states without sublattice magntization, except for the narrow Λ-shaped region in Fig. 7. There is a marked contrast between the behaviors of the easy-axis spin system we propose here to the easy-plane one proposed by Sugimoto *et al.* [17], the latter showing sublattice magnetization when considering the RKKY interaction truncated to nearest neighbors without fine-tuning the parameters as seen necessary in Fig. 7. In order to fully understand the phase diagram, one would need to extend the parameters under study, e.g., consider spin-spin correlation functions—a task beyond the scope of this paper.

B. Pure RKKY interaction

When the Hamiltonian contains the RKKY terms in Eq. (3) only, the ground-state configuration acquired from Monte Carlo simulation correlates with the sign of $u_{\rm AB}$ at a given Fermi wave vector but not with the Curie-Weiss temperature $(u_{\rm AB} + u_{\rm AA})/3$. That is, it is only the intersublattice component of the Curie-Weiss temperature that is an indicator for the magnetic ground state. In Fig. 8, we show the phase boundaries for the Heisenberg spin symmetries overlapped with $u_{\rm AB}$ and the Curie-Weiss temperature as a function of k_F. However, as in the case of the direct-exchange Hamiltonian, Eq. (2), the mean-field description only manages to capture the transitions between states with sublattice magnetization. Similarly to the experimental situation for Tb- and Gd-based approximants, we find FM and AFM phases for both Ising and Heisenberg spin symmetries under RKKY.

As in Miyazaki *et al.* [18], the Heisenberg model reaches saturation magnetization for all k_F in the FM regime. However, since both the interactions and the spin symmetry are isotropic, the model cannot select a particular direction.

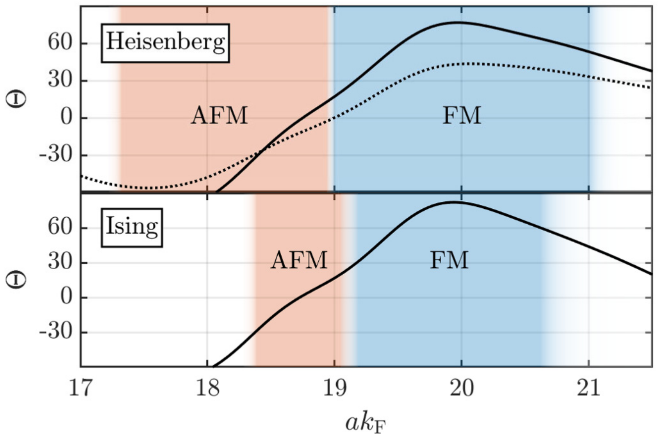

FIG. 8. Pure RKKY phase diagram. Orange (blue) color highlights the phase boundaries of the AFM (FM) states. Black lines and dotted line show Θ and $u_{\rm AB}$, respectively—the latter only defined for Heisenberg symmetry. Regions in white are without sublattice magnetization.

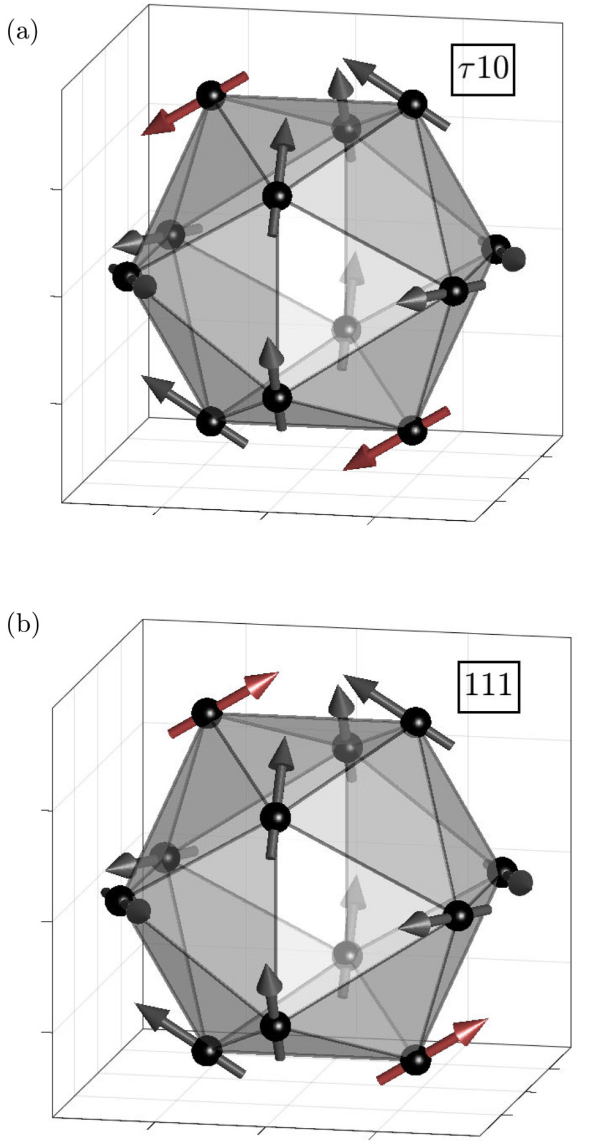

FIG. 9. Local cluster orderings in the Ising model system, denoted by the Miller indices of the net magnetization direction: (a) the $\tau10$ state and (b) the 111 state. The two spins with differing directions between the two states are highlighted in red. We find both antiferromagnetic and ferromagnetic arrangements of these cluster orderings.

Furthermore, we do not find the incommensurate regime between the FM/AFM phases reported by Miyazaki *et al.*, which could be due to us simulating a smaller system size. In the case of the Ising model, the magnetization saturates at about 53% of the Heisenberg case; see the ferromagnetic ground state in Fig. 9. The possible axes of magnetization for the Ising model ground states are found to point toward the 12 vertices of an icosahedron. Thus, we label its FM (AFM) ground states as FM $\tau10$ (AFM $\tau10$). We note that the symmetry operations relating these directions are not related to the cubic symmetry of the lattice. However, adding the dipole interaction changes this; see Sec. IV D.

For smaller k_F, both the Heisenberg and Ising models show antiferromagnetic order which is staggered along the 111 direction. The antiferromagnetic states are related to their ferromagnetic counterparts through inverting the spins located on the B clusters in the cubic unit cell; see Fig. 1. The position of the AFM/FM transition is approximately equal in both of the spin symmetries, which could be due to the long-range interactions coupling sites where the easy-axis vectors are parallel; e.g., the antipodal points in the icosahedral cluster. Thus, those Ising model correlations mimic more closely the ground states found in the Heisenberg symmetry case than under the nearest-neighbor interaction. We discuss this further in Sec. IV E.

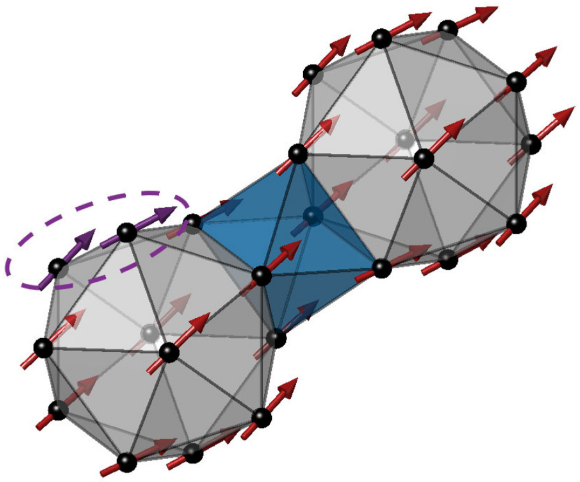

FIG. 10. Heisenberg symmetry dipole interaction ground state, neglecting the boundary term. We bring attention to the fact that the structure is not perfectly collinear; see, e.g., neighboring spins highlighted by the dashed purple ellipse.

C. Pure dipole interaction

First, we consider the ground state of the dipole Hamiltonian described by Eq. (7) with the boundary term in Eq. (19) subtracted, yielding so-called Ewald boundary conditions. This subtraction allows us to study the magnetic structure within the magnetic domains [28]. We find that Heisenberg spin symmetry yields almost collinear ferromagnetic order in the 111 direction as shown in Fig. 10. Note that this is also close to one of the ground states under the RKKY interaction, which means that there may not necessarily be a competition between these two interactions at low temperature. Enforcing Ising symmetry removes the overall magnetization, and the ground-state spin configuration features chiral order along the 111 direction; see Fig. 11. The rotation is clockwise for the A clusters and anticlockwise for the B clusters.

Since the ground state of the Heisenberg approximant model is a dipolar ferromagnet, we would expect a boundary term to lead to a low-temperature plateau in the susceptibility [28]. Indeed, on reintroducing the boundary term, we observe a minimum in $1/\chi_{zz}$ at $N = 1/3$, the demagnetization factor for a spherical sample, but note that the susceptibility rises slightly as the temperature is lowered; see Fig. 12. This behavior might be caused by the slight angular deviations from the mean magnetization axis seen in Fig. 10; another explanation could be that it is due to a finite-size effect, given that the

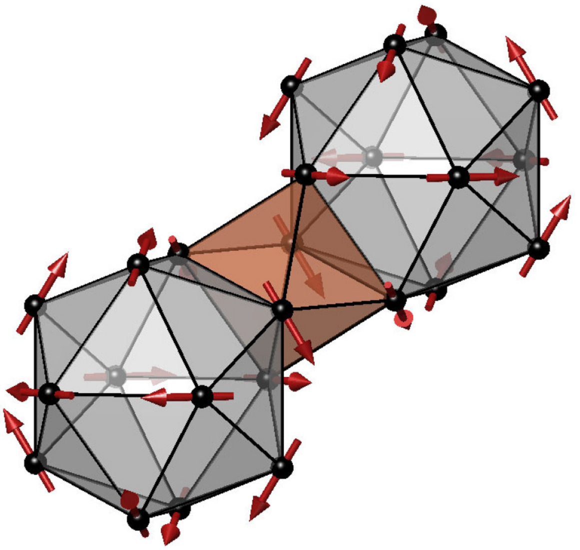

FIG. 11. Dipole interaction ground state under Ising symmetry. Note the chirality displayed by the clusters along the 111 direction.

result for $L = 5$ deviates from the smaller system sizes at low temperatures.

D. Interplay between RKKY and dipole interactions

As we found in Sec. IV B, anisotropy does not affect the AFM/FM transition point of the approximants under the RKKY interaction. This might be due to the long-range, angularly independent nature of the interaction. Therefore, we investigate the effect of breaking the global rotation symmetry by adding to the RKKY Hamiltonian, Eq. (3), a dipolar perturbation, Eq. (7), to see the effect on the phase diagram.

With a small dipole interaction alongside the RKKY interaction ($J_D/J_{\mathrm{RKKY}} = 0.1$), the Ising model displays additional ground states ordered along the 111 directions; see Fig. 13(a). The antiferromagnetic (AFM-111) and ferromagnetic (FM-111) states are related by flipping the spins located on the B cluster; see Fig. 1. The FM-111 state is shown in Fig. 14 and resembles the ferromagnetic states found in Au-Si-Tb [11,13]. The AFM-111 state have been found in both Au-Si-Ho and Au-Si-Tb compounds [21] and in Au-Al-Tb [29]. Increasing the dipole interaction to $J_D/J_{\mathrm{RKKY}} = 0.5$, the states whose

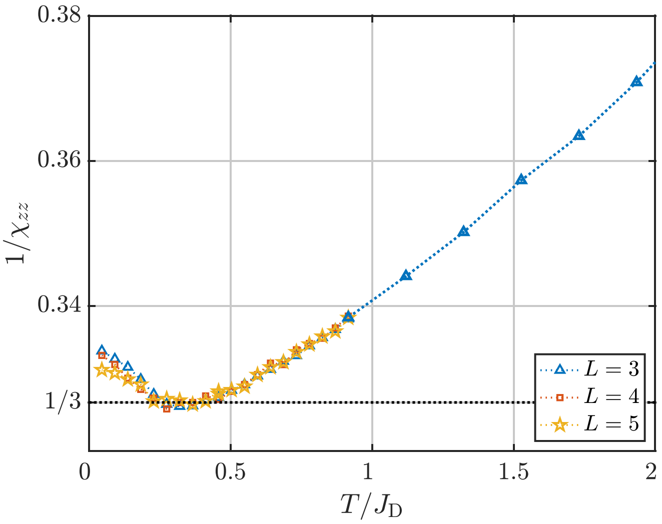

FIG. 12. Magnetic susceptibility for the dipole Hamiltonian, Eq. (7), under Heisenberg symmetry for different linear system sizes L. Note the minimum at $1/\chi_{zz} = N = 1/3$, the demagnetizing factor for a spherical sample.

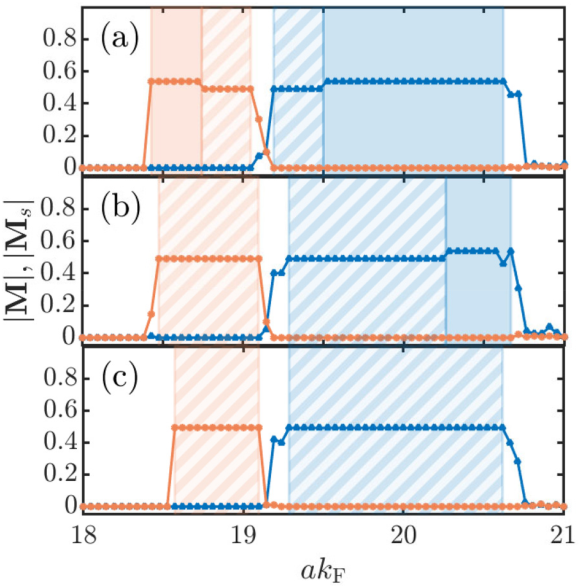

FIG. 13. Phase diagram for the Ising spin symmetry with both dipole and RKKY interactions present, FM (AFM) denoted by blue (orange), and clusterwise order 111 (τ10) by striped (single-color) boxes. Parameters: (a) $J_D/J_{\mathrm{RKKY}} = 0.1$, (b) $J_D/J_{\mathrm{RKKY}} = 0.3$, and (c) $J_D/J_{\mathrm{RKKY}} = 0.5$.

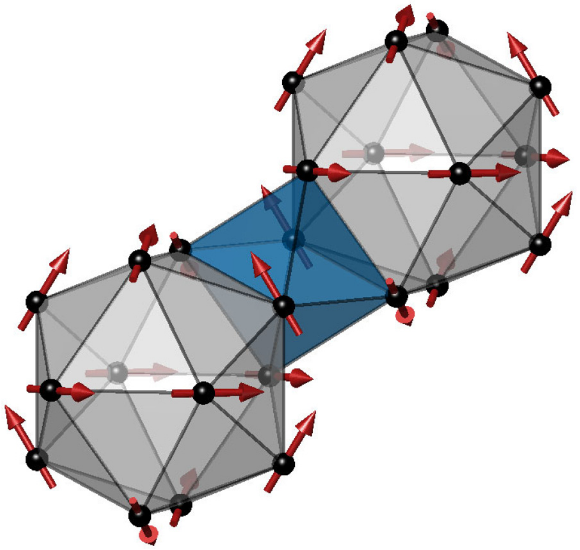

FIG. 14. The FM 111 state, so denoted since the net magnetization direction is along the 111 direction. Total magnetization at 49% of the corresponding Heisenberg ferromagnet. We bring attention to the ferromagnetic correlation between spins lying in the mirror planes of the lattice bisecting the icosahedra.

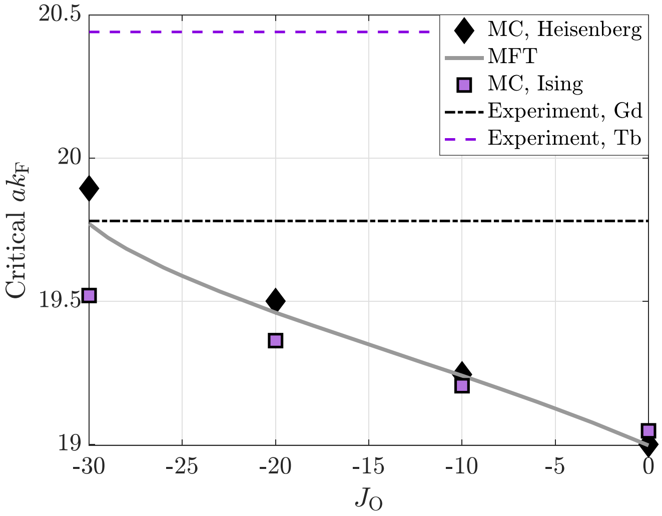

FIG. 15. Critical values for ak_F as a function of J_O. Mean field estimates from the point where u_{AB} changes sign, while keeping $T_c > 0$, Eq. (16). Since the experimental value for the critical ak_F is beyond the reaches of the models studied here, we suggest that the band structure must be taken into account when computing the RKKY couplings.

clusterwise magnetization is aligned along the $\tau 10$ directions almost disappear from the phase diagram; see Fig. 13(c). We note here that a similar effect was found by Sugimoto *et al.* [17] by adding an on-site anisotropy term.

Considering combined RKKY and dipolar interactions under Heisenberg spin symmetry leads to a similar phase diagram as in Fig. 8. However, the FM/AFM axes point along the 111 direction for arbitrarily small J_D, similarly to Fig. 10. Thus, for both Heisenberg and Ising spin symmetries, and with a dipole interaction stronger than roughly $J_D/J_{\mathrm{RKKY}} = 0.5$, the ground states are eightfold degenerate and based on our model we predict that approximants will have their magnetization axes along the 111 direction.

Experimentally, the transition between FM and AFM ground states occurs at larger electron concentrations, ν, than those observed here. As seen in Fig. 13, the critical ν_c is not affected by tuning the strength of the dipole interaction. Nevertheless, the dipole interaction seems to be important in order to acquire experimentally relevant ground states for this model.

E. Interplay between RKKY and DE interactions

As neither anisotropy nor the dipole interaction was sufficient to explain the shift between Gd and Tb approximants, we turn to the interplay between the direct-exchange and RKKY terms. Here focus lies on the only parameter in $\mathcal{H}_{\mathrm{DE}}$ that modifies the observed magnetic order, J_O.

When the intersublattice direct-exchange term $J_O < 0$, it widens the antiferromagnetic region in Fig. 8, and increases the critical value for the electron density. It also narrows the ferromagnetic region, in accordance with Eq. (16). However, assuming the relationship between k_F and ν in Eq. (6), the transition point is still for smaller ν than experimentally observed. As seen in Fig. 15, both the Heisenberg and Ising spin symmetries studied here follow roughly the estimate of the transition point computed from the mean-field theory presented in Eq. (16). The drifts for larger amplitudes $|J_O|$ are expected: The behavior should be more mean-field-like since the effective coordination number is large when H_{RKKY} dominates, as long as the model does not become frustrated. The discrepancy in the Ising case can be expected given the assumption of isotropy in deriving the mean-field results, and the fact that fixed relative angles between nearest-neighbor easy axes reduce the effective impact of J_O by a factor of $\cos\theta = \tau/(1+\tau^2) \approx 0.45$.

The different scaling of the critical Fermi wave vector versus J_O for the Heisenberg and Ising spin symmetries could explain the shift in the AFM/FM transition point between Gd- and Tb-based materials if $J_O > 0$ and taken as equal for the different materials. However, this further pushes the transition point away from the experimental value. Another explanation in the framework of our model could be that Gd- and Tb-based materials have a different J_O.

For $J_O \lesssim -10$, the FM (AFM) ground states for the Ising case have their magnetization (staggered magnetization) ordered along the $\tau 10$ directions and instead align along the 111 directions. The total magnetization per spin is again found to be 49% of that of a free ion. Thus, the addition of a nearest-neighbor interaction mimics the effect of including a dipole interaction and yields ground states reminiscent of the experimental spin structures observed in Tb-based approximant materials.

V. CONCLUSIONS

We present a systematic study of the classical magnetic properties of the 1/1 Tsai-type approximant. The key observation is that the spin symmetry in the form of Ising or Heisenberg spins does not significantly affect the Fermi wave vector at which the ground state switches from an antiferromagnet to a ferromagnet when considering the RKKY interaction. This suggests that the differences between Gd-based and Tb-based approximants stem from another source. Our results also show that the difference is most likely not due to the dipolar interaction, and a remaining possible explanation within our model is a material-dependent short-range interaction. In addition, the free-electron model might be insufficient to model the conduction band.

For the approximant we find that the key parameter determining whether the ground state is ferro- or antiferromagnetic is not the much-used Curie-Weiss temperature but rather the sign of the intersublattice mean-field u_{AB}. This is the case for the direct exchange interaction, for which u_{AB} is proportional to the direct exchange parameter J_O, and for the RKKY interaction, where the k_F dependence of u_{AB} correlates with the ground-state magnetization of both Heisenberg and Ising spin symmetries.

For Ising spin symmetry, the most significant effect of perturbing the RKKY Hamiltonian with a dipolar contribution is a slight change in the ground-state configuration. The new ground states resemble ones experimentally observed in Tb- and Ho-based approximants [11,13,21,29]. We find the that the RKKY-induced FM/AFM transition point itself is remarkably stable with respect to dipolar perturbations. On the other hand, the ground state of the approximant under Heisenberg spin symmetry and pure dipolar interaction is a ferromagnet, with an expected associated plateau in the susceptibility below the transition. We find that the plateau has a slight slope, which we believe to be caused by the noncolinear magnetic ground state. The residual gradient detected below the critical temperature resonates with similar findings reported by Tamura *et al.* [7], who observed a plateau with a slight slope at low temperatures in a newly discovered Gd-based magnetic quasicrystal. Nevertheless, it is essential to acknowledge the potential influence of a finite-size effect on our findings.

In conclusion, our study provides evidence against the hypothesis that the crystal electric field along with the nearly-free electron description of the conduction band are sufficient to explain the ground-state differences between terbium and gadolinium. It would therefore be interesting to investigate whether the anisotropy makes a difference when using a non-spherical Fermi surface to compute the RKKY couplings.

ACKNOWLEDGMENTS

We thank Cesar Pay Gomez and Johan Hellsvik for insightful discussions and Simon “Raba” Ranefjärd and Miguel Francisco Martinez Miquel for valuable input on figure design. This work has been financially supported by the Knut and Alice Wallenberg Foundation (Grant No. KAW 2018.0019). The simulations were performed on resources provided by the Swedish National Infrastructure for Computing (SNIC) at the Center for High Performance Computing (PDC) at the Royal Institute of Technology (KTH).

[1] D. Shechtman, I. Blech, D. Gratias, and J. W. Cahn, Phys. Rev. Lett. **53**, 1951 (1984).
[2] D. Levine and P. J. Steinhardt, Phys. Rev. Lett. **53**, 2477 (1984).
[3] D. Levine and P. J. Steinhardt, J. Non-Cryst. Solids **75**, 85 (1985).
[4] A. P. Tsai, J. Q. Guo, E. Abe, H. Takakura, and T. J. Sato, Nature (London) **408**, 537 (2000).
[5] H. Takakura, C. P. Gómez, A. Yamamoto, M. De Boissieu, and A. P. Tsai, Nat. Mater. **6**, 58 (2007).
[6] A. I. Goldman, Sci. Technol. Adv. Mater. **15**, 044801 (2014).
[7] R. Tamura, A. Ishikawa, S. Suzuki, T. Kotajima, Y. Tanaka, T. Seki, N. Shibata, T. Yamada, T. Fujii, C.-W. Wang, M. Avdeev, K. Nawa, D. Okuyama, and T. J. Sato, J. Am. Chem. Soc. **143**, 19938 (2021).
[8] R. Lifshitz, Mater. Sci. Eng., A **294–296**, 508 (2000).
[9] K. Inagaki, S. Suzuki, A. Ishikawa, T. Tsugawa, F. Aya, T. Yamada, K. Tokiwa, T. Takeuchi, and R. Tamura, Phys. Rev. B **101**, 180405(R) (2020).
[10] F. Labib, H. Takakura, A. Ishikawa, and R. Tamura, Phys. Rev. Mater. **6**, 124412 (2022).
[11] S. Suzuki, A. Ishikawa, T. Yamada, T. Sugimoto, A. Sakurai, and R. Tamura, Mater. Trans. **62**, 298 (2021).
[12] T. Hiroto, K. Tokiwa, and R. Tamura, J. Phys.: Condens. Matter **26**, 216004 (2014).
[13] T. Hiroto, T. J. Sato, H. Cao, T. Hawai, T. Yokoo, S. Itoh, and R. Tamura, J. Phys.: Condens. Matter **32**, 415802 (2020).
[14] M. A. Ruderman and C. Kittel, Phys. Rev. **96**, 99 (1954).
[15] T. Kasuya, Prog. Theor. Phys. **16**, 45 (1956).
[16] K. Yosida, Phys. Rev. **106**, 893 (1957).
[17] T. Sugimoto, T. Tohyama, T. Hiroto, and R. Tamura, J. Phys. Soc. Jpn. **85**, 053701 (2016).
[18] H. Miyazaki, T. Sugimoto, K. Morita, and T. Tohyama, Phys. Rev. Mater. **4**, 024417 (2020).
[19] J. M. D. Coey, *Magnetism and Magnetic Materials* (Cambridge University Press, Cambridge, UK, 2010).
[20] S. Watanabe, Sci. Rep. **11**, 17679 (2021).
[21] G. H. Gebresenbut, T. Shiino, M. S. Andersson, N. Qureshi, O. Fabelo, P. Beran, D. Qvarngård, P. Henelius, A. Rydh, R. Mathieu, P. Nordblad, and C. Pay Gomez, Phys. Rev. B **106**, 184413 (2022).
[22] C. Kittel, *Introduction to Solid State Physics*, 8th ed. (Wiley, Hoboken, NJ, 2013).
[23] N. Ashcroft and N. Mermin, *Solid State Physics*, HRW International Editions (Holt, Rinehart & Winston, New York, 1976).
[24] R. Y. Rubinstein and D. P. Koese, Markov chain monte carlo, *Simulation and the Monte Carlo Method*, 3rd ed. (John Wiley & Sons, New York, 2016), Chap. 6, pp. 187–220.
[25] Y. Miyatake, M. Yamamoto, J. J. Kim, M. Toyonaga, and O. Nagai, J. Phys. C: Solid State Phys. **19**, 2539 (1986).
[26] S. Leeuw, J. Perram, and E. Smith, Proc. R. Soc. Lond. **373**, 57 (1980).
[27] L. D. C. Jaubert, Topological constraints and defects in spin ice, Doctoral thesis, Ecole Normale Supérieure de Lyon, 2009.
[28] M. Twengström, L. Bovo, O. A. Petrenko, S. T. Bramwell, and P. Henelius, Phys. Rev. B **102**, 144426 (2020).
[29] T. J. Sato, A. Ishikawa, A. Sakurai, M. Hattori, M. Avdeev, and R. Tamura, Phys. Rev. B **100**, 054417 (2019).